Polymerization of Tspan7 into Helical Transmembrane Skeletons for Membrane Tether Stabilization

Dongju Wang[1, 2, 5], Xia Jia[1, 2, 5], Qi Zhang[1, 4], Kui Xu[1, 2, 3], Yi Zheng[1, 2], Qiangfeng Cliff Zhang[1, 2, 3], Nan Liu[1, 2*], Hong-Wei Wang[1, 2*], Li Yu[1, 2*]

[1]Beijing Frontier Research Center for Biological Structure, School of Life Sciences, Tsinghua University, Beijing 100084, China.

[2]The State Key Laboratory of Membrane Biology, Tsinghua University-Peking University Joint Centre for Life Sciences, Tsinghua University, Beijing 100084, China.

[3]Ministry of Education Key Laboratory of Bioinformatics, Center for Synthetic and Systems Biology; Beijing, 100084, China.

[4]Institute of Bio-Architecture and Bio-Interactions (IBABI), Shenzhen Medical Academy of Research and Translation, Shenzhen, China

[5]These authors contributed equally to this work.

*Correspondence: Li Yu, liyulab@tsinghua.edu.cn;

Hong-Wei Wang, hongweiwang@tsinghua.edu.cn or Nan Liu, nanliu@hku.hk

Summary

Membrane tethers, thin tubular extensions of the plasma membrane, form during cell migration, adhesion, and signaling. Various types exist, though their maintenance mechanisms are not fully understood. This study employs live cell imaging, *in vitro* reconstitution, and *in situ* cryo-EM analysis to show that Tspan7, typically a freely diffusing transmembrane protein, forms long cylindrical polymers in right-handed helical formations on retraction fibers. These polymers assemble into spiral tubule structures, acting as a "transmembrane skeleton", enriching Tspan7 on retraction fibers and promoting their formation. Our findings reveal a novel assembly strategy for transmembrane proteins and a mechanism for maintaining membrane tethers.

Keywords

Tetraspanin 7, membrane tether, *in situ* cryo-electron tomography, spiral assembly

Introduction

Membrane tethers, characterized by their dynamic, finger-like extensions from the cell membrane, are pivotal in numerous physiological and pathological contexts[1-3]. These structures, which exhibit diversity in their size, shape, and functionality, underpin critical cellular processes such as motility, tissue morphogenesis, immune function, and cancer metastasis[2,4-7]. Among these, retraction fibers stand out as slender, elongated protrusions that maintain attachment to the substrate during cellular migration, acting as mechanical tethers that facilitate both force transmission and intercellular communication[8-10]. Furthermore, retraction fibers play a key role in the formation of

migrasomes, organelles that emerge at retraction fiber junctions and tips in migrating cells, highlighting their importance in cellular signaling and material transfer[11-15]. Membrane tethers experience constant and dynamic mechanical stress. In the current model, the mechanical characteristics of these tethers are mainly determined by the dynamic of cytoskeleton, alongside their interactions with other cytoskeletal elements[2,16,17]. It remains unclear if additional structures can also influence the mechanical properties of membrane tethers.

Tetraspanins are a family of integral membrane proteins characterized by four transmembrane domains. Tetraspanins are relatively small proteins, typically ranging from 200 to 350 amino acids in length, corresponding to a molecular weight of approximately 20 to 50 kDa[18]. They play crucial roles in organizing membrane microdomains, facilitating the formation of multiprotein complexes, and influencing cell morphology[19]. Tetraspanins are involved in various cellular processes such as membrane repair, cell migration, adhesion, signal transduction[20-23] and the formation of specialized membrane structures like filopodia, microvilli, and dendritic spines[24-27]. They also function as curvature sensors and are essential for the formation and function of structures like retraction fibers and migrasomes[28-30].

Tetraspanins typically aggregate into tetraspanin-enriched microdomains on biological membranes, where they coordinate with associated proteins and specific lipids, such as cholesterol, to form nanoscale assemblies[31,32]. Additionally, certain tetraspanins, notably Tspan21/UP1a and Tspan20/UP1b, are key components of urothelial plaques[33]. These plaques consist of two-dimensional crystals with a

61 hexagonal arrangement of 16-nm protein particles on the urothelium membrane[34],
62 showcasing a different organizational strategy within the tetraspanin family for
63 structuring specialized microdomains or organized polymers on cellular membranes.

64 **Results**

65 **Tspan7 enrichment on retraction fibers**

66 Previously, we have shown that Tspan7 is required for migrasome formation[12] and that
67 its overexpression can further promote migrasome biogenesis[29], although the
68 underlying mechanism remains elusive. Given that retraction fibers are essential for
69 migrasome formation, acting both as a direct membrane source of migrasomes and as
70 a linkage between migrasomes and cell body, we were prompt to explore Tspan7's
71 potential role in retraction fiber formation. By expressing Tspan7-GFP in normal rat
72 kidney (NRK) cells, we discovered that overexpression of Tspan7 notably boosts the
73 formation of retraction fibers (Figure 1A), with cells expressing Tspan7-GFP exhibiting
74 a nearly tenfold increase in fiber length relative to those expressing GFP alone (Figure
75 1B). Similar results were also observed in other cell lines (Figure S1A-S1D).
76 Furthermore, we found that Tspan7 enhances the formation of retraction fibers in a
77 dose-dependent manner. An increase in Tspan7 expression levels correlates with more
78 retraction fibers emanating from the cells (Figure S1E-S1G).

79 Notably, Tspan7-GFP also appeared to be enriched on retraction fibers relative to
80 the cell body. To analyze Tspan7-GFP localization further, we stained NRK cells
81 expressing Tspan7-GFP with Cellmask-Deepred, which stains the plasma membrane.

By capturing images at an optical plane proximal to the cell bottom, we were able to visualize both retraction fibers and the plasma membrane on the basal side of the cell (Figure 1C). Quantitative analysis of the Tspan7-GFP and Cellmask-Deepred signals on these structures revealed that Tspan7-GFP showed much higher enrichment on retraction fibers than on the basal membrane (Figure 1D), suggesting its preference for localizing on tubular structures rather than planar membranes.

The observed preference of Tspan7 for cylindrical retraction fibers suggests its potential sensitivity to high curvature. To directly test this hypothesis, we generated Giant Plasma Membrane Vesicles (GPMVs) from Tspan7-GFP expressing cells. We then employed optical tweezers to extrude a membrane tether from a GPMV. Briefly, GPMVs were tagged with biotin-PE, and streptavidin-coated polystyrene beads were manipulated via optical tweezers to make contact with the GPMV, resulting in a strong adhesion between the streptavidin-coated bead and the biotin-PE-labeled GPMV. Moving the bead away from the GPMV facilitated the extraction of a membrane tether (Figure 1E). In this experimental setup, similar to *in vivo* observations, Tspan7-GFP was found to be highly enriched on the highly curved membrane tether compared to the GPMV, which exhibits lower curvature (Figure 1F-1I). In contrast, the Rho-PE signal was confined to the GPMV, with no obvious Rho-PE present on the membrane tether (Figure 1F, 1H). Furthermore, pannexin1, a four-pass transmembrane protein, was also found to be exclusively localized on the GPMV (Figure 1G, 1I). Collectively, these results suggest that Tspan7 has an intrinsic preference for highly curved surfaces.

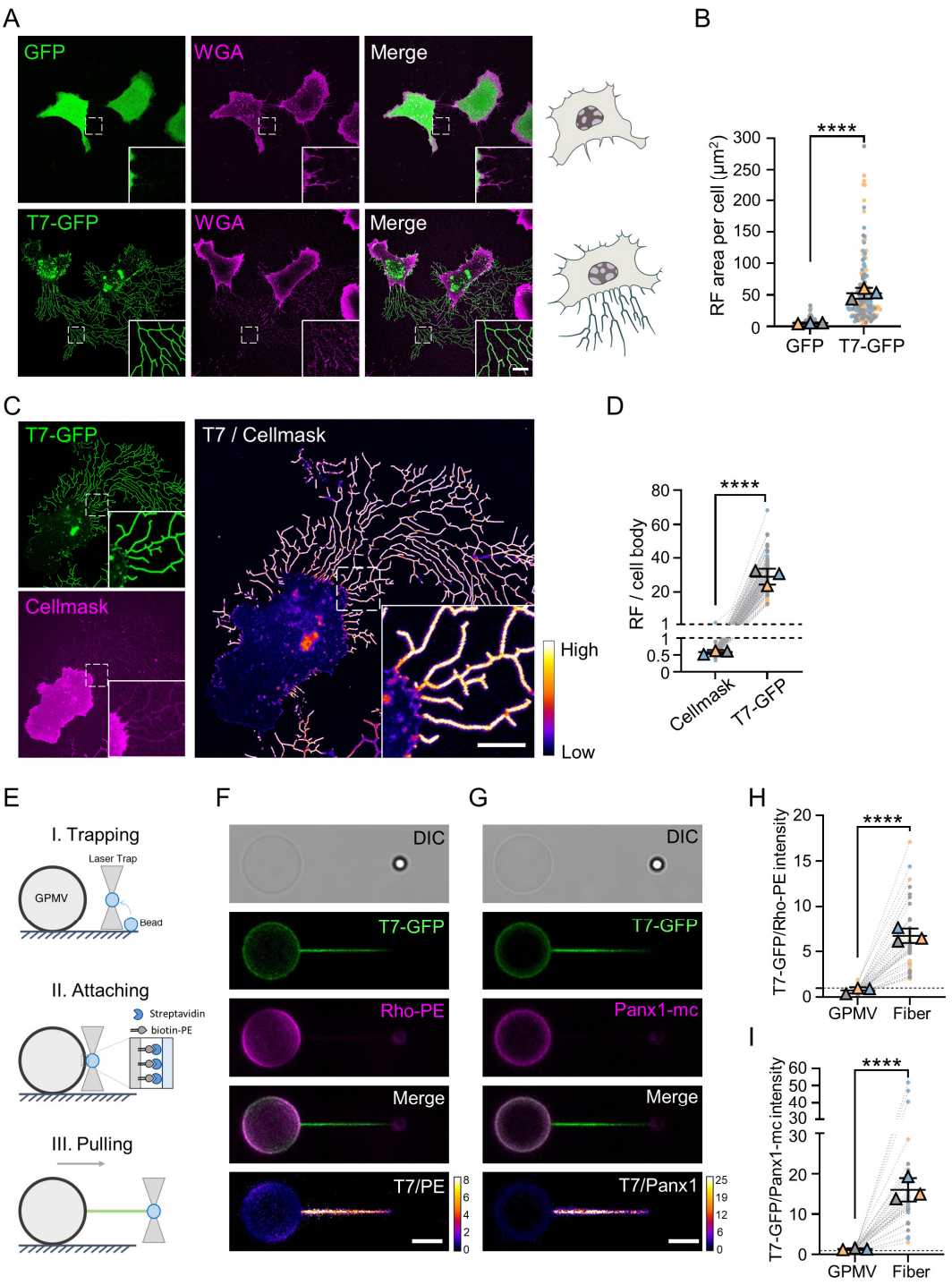

Figure 1 Tspan7 senses high curvature and promotes the formation of retraction fibers

(A, B) NRK cells transiently transfected with GFP or Tspan7-GFP (T7-GFP) were cultured on fibronectin-coated glass for 16 hours and subsequently stained with WGA-561. Representative confocal images were shown in (A) and the area of retraction fibers per cell was quantified in (B). Data from three independent experiments (colored in yellow, blue or gray respectively) was pooled,

and mean (triangles) ± SD were plotted. N = 179 and 176 cells were analyzed for GFP or T7-GFP respectively. *P* values were calculated using a two-tailed unpaired nonparametric test (Mann-Whitney test). *P* value<0.05 was considered statistically significant. **** *P*<0.0001.

(C, D) NRK cells stably expressing Tspan7-GFP were cultured on fibronectin-coated glass for 16 hours and subsequently stained with Cellmask-Deepred. Representative confocal images were shown in (C, left). The ratio of T7-GFP/Cellmask was shown in fire color map (C, right) The ratio of fluorescent intensity of Cellmask or T7-GFP on retraction fibers versus cell body was analyzed in (D). Data from three independent experiments (colored in yellow, blue or gray respectively) was pooled, and mean (triangles) ± SD were plotted. In each experiment, N = 125 cells were analyzed. *P* values were calculated using a two-tailed unpaired nonparametric test (Mann-Whitney test). *P* value<0.05 was considered statistically significant. **** *P*<0.0001.

(E) Schematic illustration of GMPV pulling assay. First, GPMVs labeled with biotin-PE were settled in a glass-bottom confocal chamber and a polystyrene bead coated with streptavidin was trapped by an optical tweezer. Next, the trapped bead was allowed to approach and contact with a GPMV by manipulating the laser trap. A strong interaction between GMPV and bead was established due to the pairing of biotin and streptavidin. Finally, a membrane tether was created by pulling the trapped bead away from GPMV. Z-stack confocal images were acquired to record the signals of fluorescent proteins or lipids on GPMV and its corresponding membrane tether.

(F, G) Representative confocal images of GPMV with a membrane tether. GPMVs were either produced by NRK cells expressing T7-GFP and stained with rhodamine-PE (F) or by NRK cells expressing T7-GFP and Pannexin1-mCherry (G).

(H, I) Statistical analysis of the fluorescent intensity of T7-GFP versus rhodamine-PE (H) or pannexin1-mcherry (I) on GPMV or fiber. Data were pooled from three independent experiments, and mean (triangles) ± SD were plotted. N = 38 and 36 GPMVs were analyzed for (H) and (I) respectively. *P* values were calculated using a two-tailed unpaired nonparametric test (Mann-Whitney test). *P* value<0.05 was considered statistically significant. **** *P*<0.0001.

Scale bars, 5 μm.

138 ***In vitro* reconstitution of Tspan7-induced membrane tethers resembling retraction**
139 **fibers**

140 To investigate Tspan7's role in membrane tether formation and avoid interference
141 from other cell components, we first purified recombinant Tspan7-GFP using a
142 mammalian expression system. Subsequently, we reconstituted Giant Unilamellar
143 Vesicles (GUVs) embedded with Tspan7-GFP *in vitro*. We discovered that when GUVs
144 made contact with a hydrophilic surface, they flattened, forming a pancake-like double-
145 membrane structure that became increasingly thin (Figure 2A). As this "pancake"
146 expanded and thinned out, the upper membrane layer eventually ruptured at its center,
147 causing the ruptured edges to retract to the pancake's periphery. This retraction left
148 behind a network of membrane tethers that closely resemble retraction fibers. As the
149 retraction process continued, vesicles began to form at the tethers' branch points. Over
150 a very short period of 390 seconds, these vesicles intensified in brightness as the tethers
151 seemingly dissolved into them (Figure 2B; Video S1), resembling the formation of
152 migrasomes. Remarkably, in GUVs incorporating Tspan7-GFP, the rupture and
153 retraction process led to an accumulation of Tspan7-GFP along the tethers, effectively
154 stabilizing them and preventing their transformation into vesicles over a relatively long
155 time (Figure 2C, 2D; Video S2). These observations confirmed that Tspan7 can detect
156 high curvature and stabilize highly curved membrane tethers (Figure 2E).
157

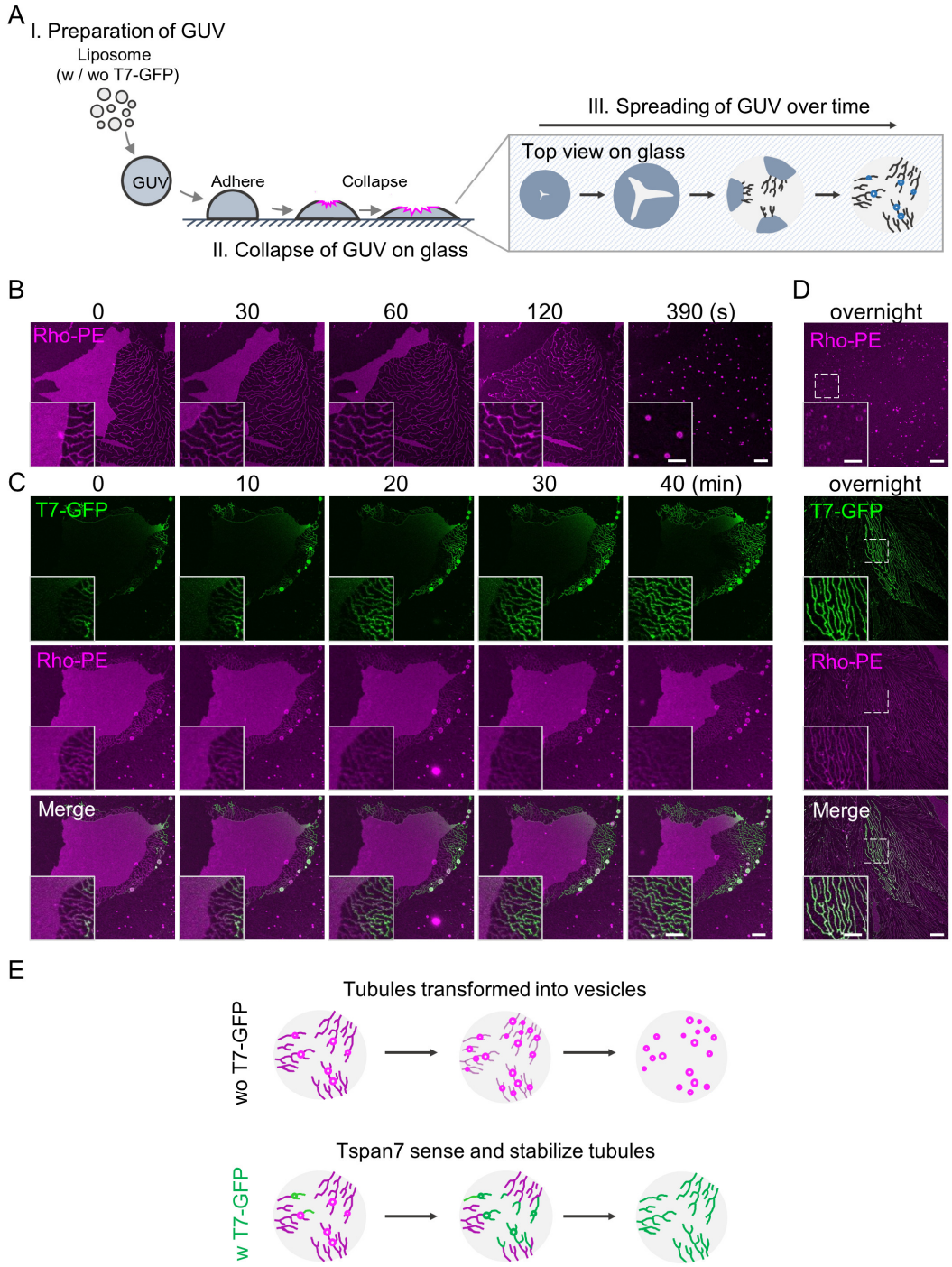

158 **Figure 2 Tspan7 senses and stabilizes tubular structures in an *in vitro* reconstitution system**

159 (A) Schematic illustration of GUV-based *in vitro* reconstitution system. Firstly, liposomes w/wo T7-
160 GFP were generated. GUVs w/wo T7-GFP were prepared from corresponding liposomes using
161 electroformation method. Next, GUVs were transferred to plasma-treated hydrophilic glass surface
162 and settled for 1.5 hour to allow attachment. Due to the strong adhesion force, the area of adhesion
163 on attached GUVs automatically expanded, resulting in the avulsion of GUV. Finally, retraction

fiber and migrasome-like structures emerged from the spreading GUVs

(B) Snapshots from a timelapse video showing the spreading of a GUV without Tspan7-GFP. See also Video S1.

(C) Snapshots from a timelapse video showing the spreading of a GUV with embedded Tspan7-GFP.See also Video S2.

(D) Representative confocal images showing the morphology of reconstitution systems after setting at room temperature overnight.

(E) Schematic illustration of the observed morphological transition of GUVs in the reconstitution system.

Scale bars,10 μm, 5 μm in inserts.

Immobility of Tspan7-GFP on retraction fibers and reconstituted RF-like membrane tethers

We next investigated whether other members of the tetraspanin family also exhibit enrichment at retraction fibers. Through phylogenetic analysis[35,36], tetraspanins can be divided into multiple subgroups (Figure 3A). We overexpressed five tetraspanins fused with GFP in NRK cells, including Tspan7-GFP, its closest homologue Tspan6-GFP and three representative members from other clusters including Tspan33-GFP, Tspan4-GFP, and Tspan27-GFP. We found that all tested tetraspanins could localize to the retraction fibers, although they showed varying preferences for retraction fibers over the flat basal plasma membranes (Figure 3B). Among these tetraspanins, Tspan7 displayed the strongest preference for retraction fibers, followed by Tspan6, which belongs to the same subgroup as Tspan7. In contrast, other tetraspanins showed relatively minor differences between their location at retraction fibers and the flat cell membranes (Figure 3B, 3C).

Interestingly, we found that the Tspan7-GFP fluorescence on retraction fibers did not recover after photobleaching (Figure 3D, 3E), suggesting that once Tspan7 is concentrated on retraction fibers, it becomes immobilized. As the closest homologue to Tspan7, Tspan6 exhibited partial recovery after photobleaching. In contrast, tetraspanins belonging to other subgroups showed a rapid and nearly complete signal recovery after photobleaching (Figure 3D, 3E). This distinctive behaviour of Tspan7,which includes its unique immobility on retraction fibers, is intriguing for a small membrane protein and deviates from what is typically expected. Subsequently, we assessed the mobility of Tspan7-GFP on *in vitro* reconstituted membrane tethers. Our findings revealed that Tspan7-GFP remained immobile (Figure 3F, 3G), similar to *in vivo* observations. Given that the *in vitro* system consists solely of Tspan7-GFP and lipids, this result suggests that the immobility of Tspan7 is an intrinsic property, not a consequence of interactions with other proteins.

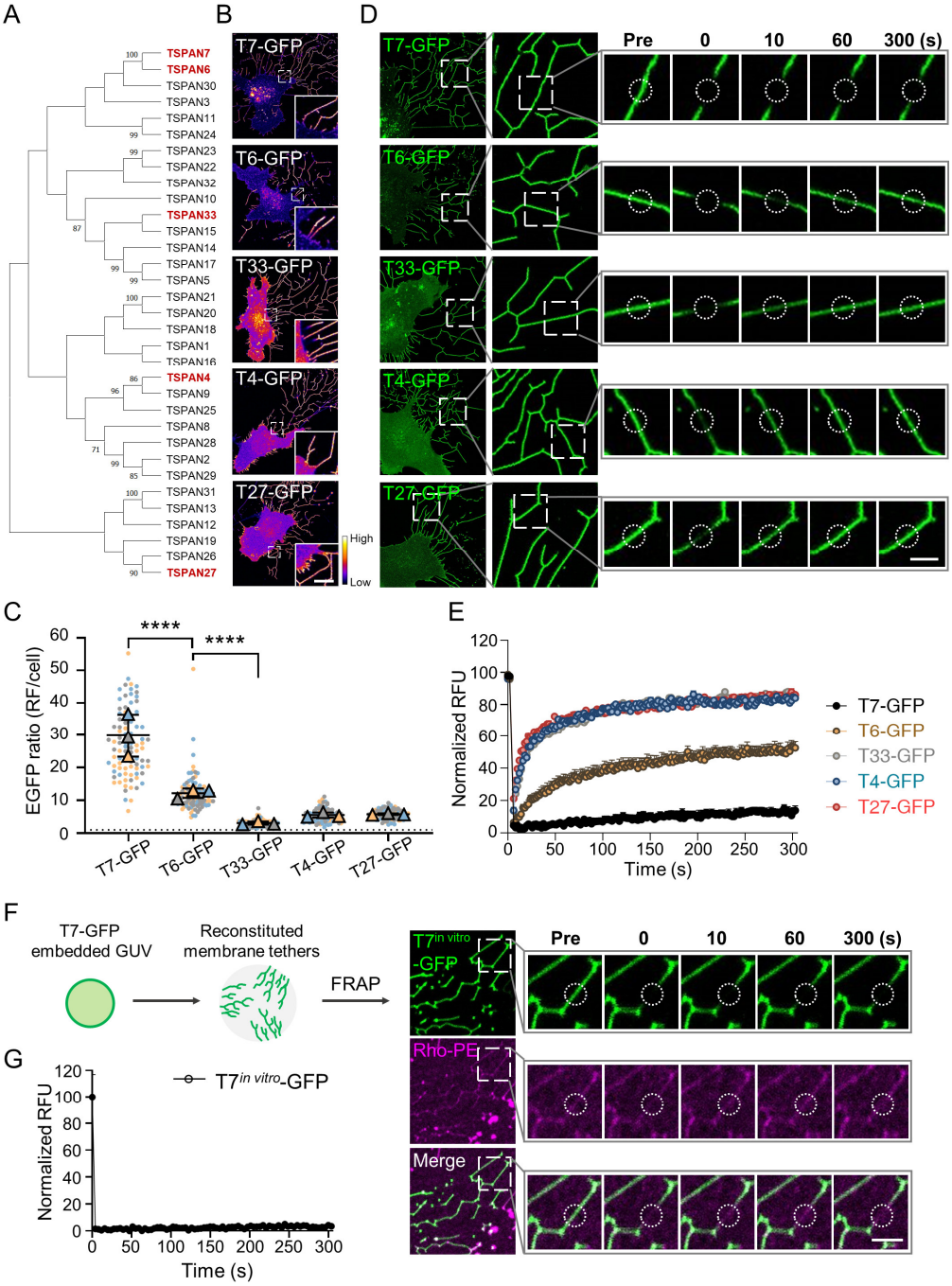

Figure 3 Immobility of Tspan7-GFP on retraction fibers and reconstituted RF-like membrane tethers

(A) Phylogenic tree of tetraspanin family generated by MEGA11. First, the protein sequences of 33 human tetraspanins were aligned using MUSCLE algorithm. Then, a phylogenic tree was constructed using Maximum Likelihood method. Bootstrap method with 1000 replications was used to test phylogeny. Frequencies with values higher than 70% were labeled at each branch. Five tetraspanins were highlighted in red: TSPAN7; its closest homologue TSPAN6 and representative

210 tetraspanins from three different clusters TSPAN33, TSPAN4 and TSPAN27.

211 (B-E) NRK cells were transiently transfected with Tspan7-GFP (T7-GFP), Tspan6-GFP (T6-GFP),
212 Tspan27-GFP (T27-GFP), Tspan4-GFP (T4-GFP) or Tspan33-GFP (T33-GFP) and cultured on
213 fibronectin-coated glass overnight. The fluorescent intensity of GFP was shown in fire color map in
214 (B) and the ratio of GFP intensity on retraction fiber (RF) versus cell was analyzed in (C). Data
215 from three independent experiments (colored in yellow, blue or gray respectively) was pooled, and
216 mean (triangles) ± SD were plotted. N = 90 cells were analyzed for each group. *P* values were
217 calculated using a two-tailed unpaired nonparametric test (Mann-Whitney test). *P* value<0.05 was
218 considered statistically significant. **** *P*<0.0001.

219 (D, E) FRAP assays were performed on transfected cells in order to analyze the mobility of different
220 tetraspanins on retraction fibers. Representative time-lapse images were shown in (D). The right
221 panels represent enlarged area from the left panels. The dashed circles represent areas of bleaching.
222 A 5-minute movie was acquired after bleaching. Representative images before or after bleaching
223 were shown. The fluorescent intensity in bleached area were tracked and plotted in (E). For each
224 curve, data from 15 bleaching areas were normalized and plotted as mean + SEM.

225 (F, G) FRAP assays were performed on *in vitro* reconstituted fibers as described in Figure 2. Time
226 lapse images before and after bleaching were shown in (F). Dashed circles represent areas of
227 bleaching. The GFP intensity in bleached area were tracked and plotted in (G). Data from 9
228 bleaching areas were normalized and plotted as mean + SEM.

229 Scale bars, 5 μm in (B); 2 μm in (D) and (F).

230

231 Cryo-EM revealed the highly ordered spiral assembly of Tspan7 on retraction 232 fibers

233 As a small transmembrane protein (28 kDa), Tspan7 is expected to diffuse
234 relatively freely on the membrane and recover quickly after photobleaching, similar to
235 other tetraspanins. But our observation is against this notion. One possible explanation
236 for its differing behavior is that Tspan7 forms higher-order oligomers on retraction

237 fibers. We then sought to explore the structural basis of Tspan7's immobility on
238 retraction fibers. For this purpose, we performed *in-situ* cryo-EM analysis on NRK cells
239 overexpressing either Tspan7-GFP or Tspan4-GFP, the latter serving as a control due to
240 its high mobility on retraction fibers (Figure 3D, 3E). Briefly, NRK cells were seeded
241 and cultured overnight on EM grids. We captured the fluorescent images of the cells to
242 identify retraction fibers with strong green fluorescence signals. The EM grids were
243 then rapidly frozen for cryo-EM imaging. Starting with a low-magnification cryo-EM
244 micrograph, we correlated it with the fluorescent cell images to pinpoint the target
245 retraction fibers. We then switched to high-magnification mode to capture detailed
246 structural information of the retraction fibers (Figure 4A).

247 We firstly collected the cryo-EM micrographs of retraction fibers and performed
248 single particle averaging analysis to sort relatively homogenous structures and enhance
249 the signal-to-noise ratio of them (Figure 4B). We found that certain portion of retraction
250 fibers overexpressing Tspan7-GFP exhibited a more uniform diameter of approximately
251 25 nm. Notably, we observed a regular row of dots, each about 5 nm in size, along the
252 cytoplasmic side of these group of Tspan7-GFP retraction fibers (Figure 4B, bottom), a
253 feature absent in those overexpressing Tspan4-GFP (Figure 4B, top). We then collected
254 the tilt series of the retraction fibers in cryo-EM and reconstructed their cryo-eletron
255 tomograms. Analysis of the tomograms confirmed the presence of the same regular row
256 of dots along the inner side of Tspan7-GFP retraction fibers, a feature not observed in
257 Tspan4-GFP retraction fibers (Figure 4C, 4D), consistent with the single-particle
258 analysis.

259 We hypothesized that the observed dots corresponded to the GFP tags (27 kDa)
260 fused to the C-terminus, that is, the cytoplasmic side of the Tspan7 protein, as their size
261 matched well with that of GFP proteins. To test this, we replaced the GFP tag at the
262 cytoplasmic C-terminal of Tspan7 with a much smaller HA tag consisting of only nine
263 amino acids. This substitution caused the regular dot pattern on the cytoplasmic side to
264 disappear (Figure 4E, right). These results collectively confirm that the dot pattern is
265 linked to the GFP protein, serving as an indicator for the positioning and arrangement
266 of Tspan7, which displayed a highly ordered and densely packed configuration on the
267 retraction fibers.

268 Interestingly, cryo-EM tomography analysis revealed a spiral arrangement in the
269 Tspan7-GFP retraction fibers (Figure 4E, middle; Figure S2C, S2D; Video S4). In
270 contrast, the Tspan4-GFP retraction fibers, which are highly mobile, did not show spiral
271 structures (Figure 4E, left; Figure S2A, S2B; Video S3). This finding, along with
272 previous observations, indicates that Tspan7 concentrates and forms a highly ordered
273 spiral structure on retraction fibers. The similar spiral arrangement was also observed
274 on retraction fibers from cells overexpressing Tspan7-HA (Figure 4E, right; Video S5),
275 though these fibers were narrower compared to those expressing Tspan7-GFP,
276 suggesting that the diameter of Tspan7-containing fibers may be influenced by the tag
277 size. This result indicates that the formation of the spiral structure is an intrinsic
278 property of Tspan7, independent of its labeling constructs. Segmentation of the Tspan7-
279 GFP spiral structure revealed a right-handed six-start spiral with a diameter of 25 nm
280 (Figure 4F; Figure S3), exhibiting varying helical parameters.

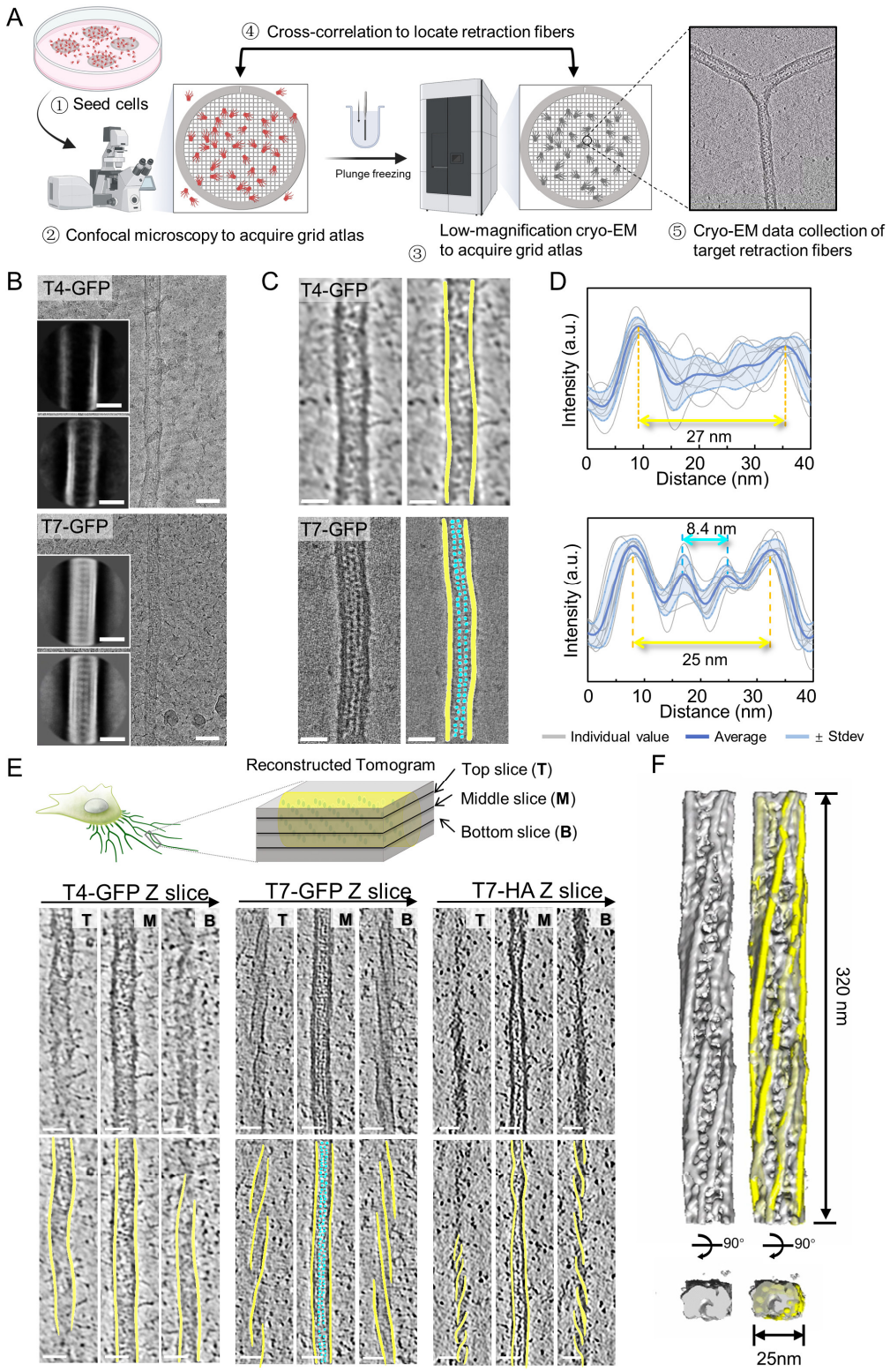

Figure 4 Cryo-EM analysis of Tspan7 arrangement on retraction fibers

(A) Diagram of cryo-EM sample preparation and data collection. We first seed cells on golden EM grids coated with graphene film (Step 1) and use a confocal fluorescent light microscope (fLM) to take images of the cells (Step 2). After that, the cells cultured on EM grids would be blotted from

285 their backside and quickly frozen into liquid ethane to prepare the cryo-specimen. The atlas of EM
286 grid was captured and cross-correlated with the fluorescent images in step 2, to locate the target
287 retraction fibers (step 4). Tilt series or single-particle datasets were then acquired at the desired
288 regions (step 5).
289 (B) Two-dimensional (2D) average results of particles picked from the cryo-EM micrographs of
290 Tspan4-GFP (top) and Tspan7-GFP (bottom) retraction fibers.
291 (C) Representative central slices extracted from the tomogram reconstructions of Tspan4-GFP (top)
292 and Tspan7-GFP (bottom) retraction fibers. The right panels showed the central slices with the
293 membrane labeled in yellow and the dots in cyan.
294 (D) The intensity of the 9 line cross-sections across the Tspan4-GFP (top) and Tspan7-GFP (bottom)
295 retraction fibers, plotted as a function of distance. The dark blue line was the averaged trace for all
296 plots. The light blue line was the averaged trace after adding or subtracting the standard deviation.
297 The distances separating the peak maxima were indicated for membrane densities (yellow line) and
298 luminal dot densities (cyan line). a.u., arbitrary units.
299 (E) Representative bottom (B), middle (M), and top (T) slices of Tspan4-GFP (left), Tspan7-GFP
300 (middle) or Tspan7-HA (right) retraction fiber tomograms. The yellow lines outlined the cell
301 membrane in different slices, and the cyan markers indicated the regular dot density attached to the
302 cytoplasmic side of the cell membrane. See also Video S3, S4, and S5.
303 (F) On the left, a typical density of a Tspan7-GFP retraction fiber segmented from the tomogram
304 reconstruction. On the right, the density was identified as a right-handed six-start helix, with the six
305 individual strands indicated by the six yellow lines.
306 Scale bars, 30 nm.
307

308 **The formation of the Tspan7 spiral structure is negatively regulated by**
309 **filamentous actin**

310 We further examined the distribution and assembly of Tspan7 on retraction fibers
311 at varying distances from the cell bodies, from proximal to distal (Figure 5A). In the

312 proximal region, where membrane curvature starts to increase, densely distributed GFP
313 dots were absent along the cytoplasmic side of the plasma membrane, and no spiral
314 arrangement was observed (Figure 5B, upper). Conversely, in the distal region, densely
315 distributed GFP dots along with a spiral arrangement were visible (Figure 5B, middle
316 and bottom), suggesting a preferential distribution of Tspan7 on the distal region. This
317 observation is consistent with our earlier findings that Tspan7 favors highly curved
318 membrane regions (Figure 1).

319 Filamentous actin (F-actin) is frequently observed in the proximal region of
320 retraction fibers[11]. To investigate the possible interplay between Tspan7 and F-actin
321 within these regions, cells expressing Tspan7-GFP were stained by SiR-actin, a
322 fluorescent probe for F-actin. We found that F-actin is predominantly located in the
323 proximal region of the retraction fibers, with occasional presence in isolated short
324 sections of the distal region (Figure 5C). Colocalization analysis of Tspan7-GFP and
325 SiR-actin signals on retraction fibers showed that these two components have a negative
326 correlation (Figure 5D). The repulsion between the distribution of F-actin and Tspan7-
327 GFP signals in the proximal region is further depicted by time-lapse analysis,
328 characterized by an increase in F-actin fluorescence coinciding with a decrease in
329 Tspan7-GFP fluorescence within the same area (Figure 5E; Video S6). In regions with
330 strong F-actin fluorescence, Tspan7-GFP fluorescence is often undetectable. When both
331 F-actin and Tspan7-GFP are present, their signals are generally weak. Photobleaching
332 experiments in areas with both signals suggest partial recovery of Tspan7-GFP
333 fluorescence, indicating some degree of diffusion of Tspan7-GFP in these regions

334 (Figure 5F, 5G). Collectively, these observations imply that the presence of F-actin in
335 retraction fibers may hinder Tspan7 recruitment and limit the formation of Tspan7 spiral
336 structures.

337 Next, we treated Tspan7-GFP expressing cells with Latrunculin A (LatA) to disrupt
338 F-actin assembly. LatA treatment did not affect the immobile state of Tspan7-GFP
339 (Figure 5H, 5I). Cryo-EM tomography analysis revealed a tightly packed Tspan7
340 configuration and spiral structure in LatA-treated retraction fibers (Figure 5J; Figure
341 S2E, S2F; Video S7). We then calculated the percentage of spiral formation in LatA-
342 treated Tspan7 retraction fibers and non-treated Tspan7 retraction fibers. This was
343 determined by the ratio of the number of retraction fibers exhibiting an obvious spiral
344 structure to the total number of retraction fibers. We found that LatA treatment
345 significantly increased the formation of Tspan7 spirals, from 24% to 88%, compared to
346 the untreated samples (Figure 5K). Furthermore, we also quantified the tightness of the
347 spiral structure using an angular velocity metric, defined as the ratio of the twist angle
348 to the rise of the spiral. This angular velocity metric also changed significantly, shifting
349 from 0.99 to 1.29 °/nm after LatA treatment (Figure 5L). This indicates that the Tspan7
350 spiral adopted a tighter form when the F-actin fiber was absent (Figure 5M). Together,
351 these data confirm that the presence of F-actin hinders the formation of Tspan7-GFP
352 spirals.

353

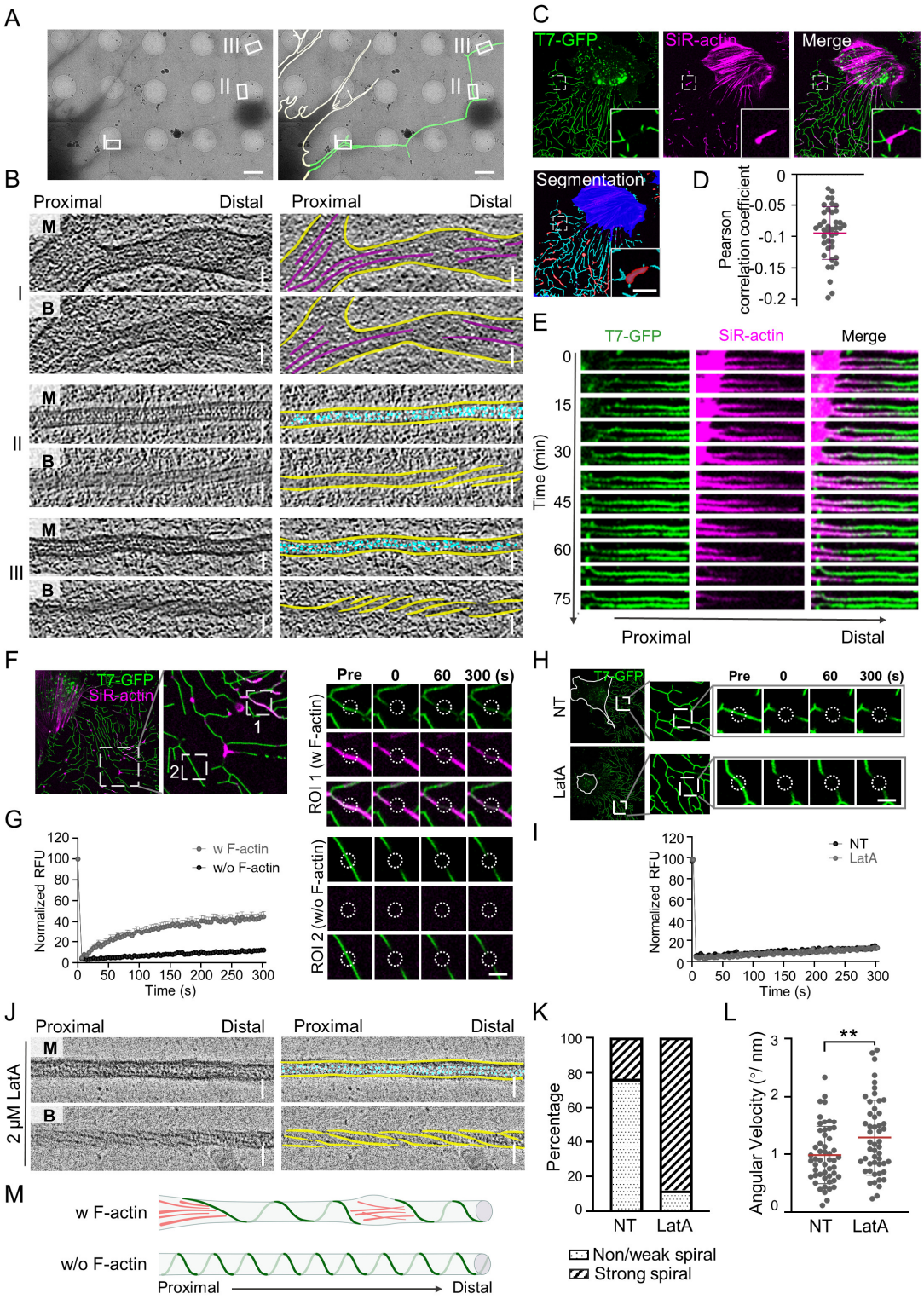

354 **Figure 5 The interplay between Tspan7 and F-actin**

355 (A) On the left, a representative low-magnification cryo-EM micrograph shows retraction fibers
356 extruding from the cell body. On the right, the cell boundary is traced using white lines and the
357 retraction fibers are indicated with green lines.

358 (B) The left panel displays the middle (M) and bottom (B) slices of the tomograms, corresponding
359 to the three areas labeled as I-III in (A). On the right, F-actin is labeled in magenta, the cell
360 membrane is labeled in yellow, and GFP is labeled in cyan.
361 (C) Representative confocal images of NRK cells stably expressing Tspan7-GFP, which had been
362 stained with SiR-actin prior to imaging. In the segmentation image, cell body, total retraction fibers
363 and SiR-actin-positive areas on retraction fibers were colored in deep blue, cyan and red respectively.
364 (D) The Pearson correlation coefficient of Tspan7-GFP and SiR-actin on retraction fibers was
365 calculated based on the segmented images in (C). N=40 images were analyzed. Values between 0
366 and -0.3 indicate weak negative correlations.
367 (E) Snapshots from a timelapse video of a migrating cell. See also Video S6.
368 (F) Representative confocal images of NRK cells in order to analyze the mobility of Tepans7 on
369 retraction fibers. The right panels represent enlarged area from the left panels (top: ROI 1, bottom:
370 ROI 2). The dashed circles represent areas of bleaching. A 5-minute movie was acquired after
371 bleaching. Representative images before or after bleaching were shown. ROI: Region Of Interest.
372 (G) The fluorescent intensity in bleached areas in (F) were tracked and plotted. For each curve, data
373 from 15 bleaching areas were normalized and plotted as mean + SEM.
374 (H, I) FRAP assays were performed on NRK cells stably expressing tspan7-GFP. Cells were
375 pretreated with 2 μM latrunculin A (LatA) or control solvent ethanol (NT). Confocal images of cells
376 before FRAP assay were shown in (H), contour of the cells were highlighted in white line. The right
377 panels represent enlarged area from the left panels. The dashed circles represent areas of bleaching.
378 A 5-minute movie was acquired after bleaching. Representative images before or after bleaching
379 were shown. The fluorescent intensities in bleached area were tracked and plotted in (I). For each
380 curve, data from 15 bleaching areas were normalized and plotted as mean + SEM.
381 (J) The middle (M) and bottom (B) slices of the tomogram of tspan7-GFP retraction fibers after
382 LatA treatment. See also Video S7.
383 (K) Statistical analysis on the formation of Tspan7 spiral after LatA treatment. N=75 or 51
384 tomograms of Tspan7-GFP retraction fibers that were either nontreated (NT) or treated with LatA
385 were analyzed, respectively. Retraction fibers were categorized as either "non/weak spiral",
386 indicating no spiral or a very slight spiral that was difficult to identify, or "strong spiral", indicating

387 a very obvious spiral structure on the retraction fibers.

388 (L) Plotting of the angular velocity of the Tspan7 spirals to assess their tightness. We analyzed N=52

389 randomly selected spiral structures (each around 30nm in length) from Tspan7-GFP retraction fibers

390 that were either nontreated (NT) or treated with LatA. The means (dark red line) ± SD were plotted.

391 *P* values were calculated using a two-tailed unpaired nonparametric test (Mann-Whitney test). A *P*

392 value <0.05 was considered statistically significant. ** *P*<0.01

393 (M) Model showcasing the assembly state of Tspan7 spirals on retraction fibers with or without the

394 existence of F-actin.

395 Scale bars, 1 μm in (A); 30 nm in (B); 5 μm in (C); 2 μm in (F) and (H).

396

397 **Structural analysis of Tspan7 spiral on retraction fiber**

398 Tspan7-GFP retraction fibers exhibited a more uniform diameter and a higher

399 density of GFP "dot" compared to Tspan7-HA retraction fibers (Figure 4E). As a result,

400 we chose Tspan7-GFP retraction fibers for subsequent cryo-EM subtomogram

401 averaging (STA) analysis to elucidate more detail information of the Tspan7 spiral

402 structure and identify critical interaction interfaces within the spiral.

403 The STA reconstruction of Tspan7-GFP retraction fibers revealed the general spiral

404 shape (Figure S3C). A higher resolution reconstruction was hindered by the

405 heterogeneity of the Tspan7-GFP spiral assembly in the retraction fibers (Figure 6B).

406 The resulting spiral density revealed a right-handed six-start helix with a twist of 3.14°

407 and a rise of 6.5 nm, with the GFP densities located in the center of the cylindrical

408 retraction fiber.

409 To pinpoint the potential key residues on Tspan7 that contribute to the formation

410 of spiral structure on retraction fibers, we utilized AlphaFold-Multimer[37,38] to predict
411 multiple hypothetical models of Tspan7 dimers (Figure 6A; Figure S4, S5). By
412 analyzing the interaction interfaces, we clustered these Tspan7 dimers into 5 distinct
413 classes and then selected a representative dimer model from each class (Figure S5) to
414 dock into the STA density. After correlating the models with the cryo-EM density map
415 of Tspan7 spiral, two of the dimer models, dimer 1 and dimer 2, exhibited the best
416 matches to the Tspan7 spiral structure. Following density-guided adjustment, we built
417 a putative model of how Tspan7 assembles into a spiral along the retraction fiber, using
418 the interaction interfaces observed in dimer 1 and dimer 2 (Figure 6B). In this model,
419 six strands of Tspan7 form a right-handed spiral, where the two interaction interfaces
420 between adjacent Tspan7 monomers are oriented in a head-to-head and back-to-back
421 arrangement, facilitating the organization of Tspan7 protomers within each strand.

422 To verify the above-built model of Tspan7 in the spiral, we performed a
423 comprehensive mutation analysis of the interaction interfaces to identify critical
424 residues in Tspan7 that contribute to its spiral arrangement and immobility (Figure 6C,
425 S7A). Our analysis pinpointed several key sites responsible for Tspan7's immobility,
426 including E115, aa190-199 (TVAATKVNQK) in the large extracellular loop, and aa53-
427 57 (ENSTN) in the small extracellular loop (Figure 6C). In cells expressing Tspan7-
428 GFP with mutations E115A, Δ53-57, or Δ190-199, immobility was partially lost. In
429 contrast, cells expressing the triple mutant Tspan7-GFP-E115A, Δ53-57, Δ190-199 (T7
430 3M) showed almost complete loss of immobility, suggesting that T7 3M cannot form
431 spirals. To further validate our findings, we performed in situ cryo-tomography analysis

432 on retraction fibers overexpressing T7 3M and found that the spiral structure was indeed
433 absent (Figure 6D; Video S8). Moreover, sequence alignment revealed that these
434 identified interaction sites are fully conserved in mouse and human Tspan7 (Figure
435 S6B). Among these sites, E115 is conserved in Tspan6 but not in Tspan4, aa53-57 and
436 aa190-199 are not conserved in Tspan6 or Tspan4 (Figure S6A). These results indicate
437 that the identified interaction interfaces are crucial for Tspan7's oligomerization and
438 spiral assembly on retraction fibers.

439 Finally, we compared the enrichment of Tspan7 WT-GFP and Tspan7 3M-GFP on
440 retraction fibers. Compared to Tspan7 WT-GFP, Tspan7 3M-GFP showed significantly
441 reduced enrichment on retraction fibers (Figure 6E, 6F). Moreover, in cells expressing
442 Tspan7 3M-GFP, the retraction fibers were significantly shorter than those in cells
443 expressing Tspan7 WT-GFP (Figure 6G, S7B). This suggests that spiral formation is
444 crucial for the enrichment of Tspan7 on retraction fibers and for maintaining their length.
445

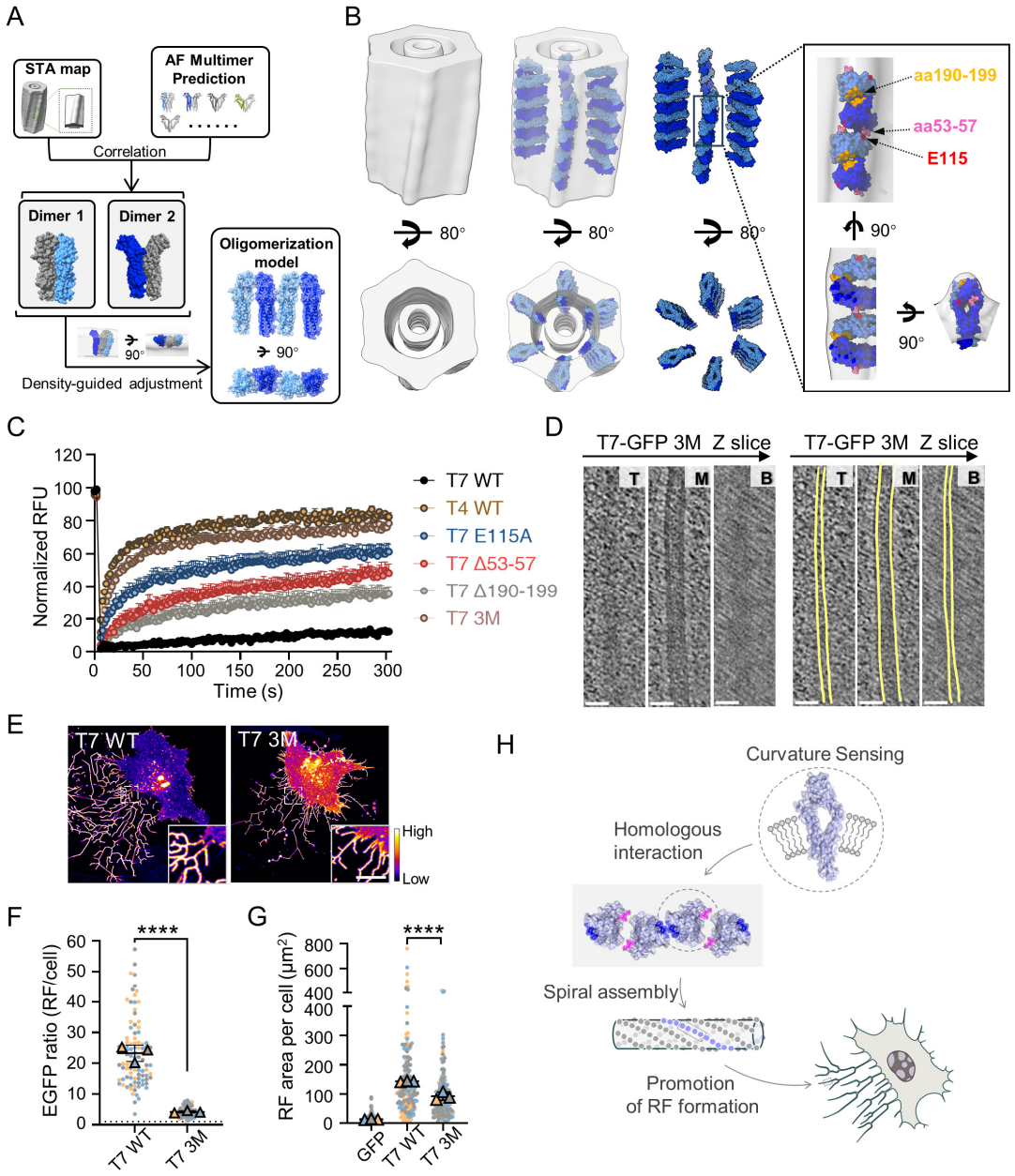

Figure 6 Construction and verification of the molecular model of Tspan7 spiral

(A) The process of generating Tspan7 oligomerization models by combining the EM density map and the AlphaFold-Multimer structural prediction.

(B) Subtomogram average of the Tspan7-GFP retraction fiber and the fitting of the helical model to the map. The potential interaction surfaces involved in the oligomerization of Tspan7 (aa190-199, aa53-57, and E115) were also highlighted.

(C) NRK cells were transiently transfected with wild-type Tspan7-GFP (T7 WT), wild-type Tspan4-GFP (T4 WT), single-site mutant Tspan7-GFP (T7 E115A, T7 Δ53-57, T7 Δ190-199) and multiple-sites mutant Tspan7-GFP (T7 3M with triple mutations E115A, Δ53-57 and Δ190-199). FRAP assays

were performed on transfected cells in order to analyze the mobility of WT or mutant tetraspanins on retraction fibers (See also Figure S7A.) For each curve, data from 15 bleaching areas were normalized and plotted as mean + SEM.

(D) Representative tomogram slices of the mutated Tspan7-GFP retraction fibers (T7 3M with triple mutations E115A, Δ53-57 and Δ190-199). See also Video S8.

(E, F) NRK cells were transiently transfected with wild-type Tspan7-GFP (T7 WT) or mutant Tspan7-GFP (T7 3M). The fluorescent intensity of GFP was shown in fire color map in (E) and the ratios of GFP intensity on retraction fiber (RF) versus cell were analyzed in (F). Data from three independent experiments (colored in yellow, blue or gray respectively) was pooled, and mean (triangles) ± SD were plotted. N = 94 and 92 cells were analyzed for WT and mutant respectively. *P* values were calculated using a two-tailed unpaired nonparametric test (Mann-Whitney test). *P* value<0.05 was considered statistically significant. **** *P*<0.0001.

(G) NRK cells transiently transfected with GFP, wild-type Tspan7-GFP (T7 WT) or mutant Tspan7-GFP (T7 3M) were cultured on fibronectin-coated glass for 16 hours and subsequently stained with WGA-561 (See also Figure S7B). The area of retraction fibers per cell was quantified. Data from three independent experiments (colored in yellow, blue or gray respectively) was pooled, and mean (triangles) ± SD were plotted. N = 167, 174 and 181 cells were analyzed for GFP, T7 WT and T7 3M respectively. *P* values were calculated using a two-tailed unpaired nonparametric test (Mann-Whitney test). *P* value<0.05 was considered statistically significant. **** *P*<0.0001.

(H) Working model of the transmembrane skeleton Tspan7. Tspan7 monomers sense high membrane curvature, forming polymers via homologous interaction on membrane tethers. When the cytoskeleton retracts, the Tspan7 polymers shape and stabilize the membrane tether through spiral assembly.

Scale bars, 30 nm in (D); 5 μm in (E).

Discussion

In this study, we have identified that Tspan7 is highly concentrated on retraction fibers and reconstituted membrane tethers. Our results revealed that Tspan7's selective

association with retraction fibers stems from its capacity to sense and concentrate on the highly curved membrane tethers. This accumulation is significantly amplified when Tspan7, typically a freely diffusing small transmembrane protein, organizes into long cylindrical polymers, adopting right-handed helical formations. We demonstrated that on retraction fiber, Tspan7 assembles into a tubular six-start spiral structure. Further, our findings indicate that these Tspan7 tubules markedly enhance the length of retraction fibers, and substantially improve their stability. Given the structural parallels between Tspan7 tubules and microtubules — both composed of polymerized basic protein units forming linear protofilaments and both providing structural support — we suggest that Tspan7 tubules act as a form of "transmembrane skeleton". This transmembrane skeleton, akin to the cytoskeleton, not only offers structural support but may also fulfill various other roles.

Membrane tethers, such as filopodia, retraction fibers, tunneling nanotubes, and microvilli, are prevalent features across various specialized cells and play critical roles in physiological processes. A shared characteristic of these protrusions is their exposure to constant mechanical stress, highlighting the potential benefit of a transmembrane skeleton that can stabilize these structures. Whether Tspan7 tubules can form and stabilize different types of membrane tether, or whether other proteins can create a transmembrane skeleton using similar organizational principles, remains to be determined.

Consistent with our previous finding, we found that Tspan7 overexpression not only elongates retraction fibers but also promotes migrasome formation. Earlier studies

505 suggested that the assembly of tetraspanin-enriched macrodomains triggers migrasome
506 formation. We observed that Tspan4, a non-polymerizing tetraspanin, integrates into
507 nanometer-scale tetraspanin microdomains and preferentially assembles in migrasomes
508 over retraction fibers[29]. This study, however, shows that Tspan7 has a contrasting
509 distribution, being more concentrated on retraction fibers. Considering the extensive
510 coverage of the Tspan7 transmembrane skeleton on retraction fibers, we propose that
511 Tspan7 facilitates migrasome formation by spatially restricting the movement of
512 tetraspanin-enriched microdomains, effectively channeling them towards migrasomes
513 and supporting their formation. Further research is required to test this hypothesis.

514 The absence of a functional Tspan7 antibody prevents us from directly testing the
515 formation of endogenous Tspan7 tubules. However, our data suggest that the assembly
516 of Tspan7-GFP tubules is not merely due to GFP's propensity for dimerization, as
517 replacing the GFP tag with an HA tag does not affect Tspan7's ability to form spiral
518 tubules, and mutating the potential interaction sites on Tspan7 abolishes the spiral
519 formation. Based on these findings, we think that Tspan7 tubules are likely a genuine
520 structure.

521 Except for a few cases, investigating cellular structures ranging from 10 nm to 100
522 nm has previously been challenging. Traditional structural biology tools are difficult to
523 implement *in vivo*, and optical imaging lacks the necessary resolution. Recently,
524 advancements in cryo-electron tomography (cryo-ET) have shown potential to change
525 this scenario. However, cryo-ET faces several challenges, including inherently low
526 signal-to-noise ratio and a limited field of view, which make searching for ordered

cellular structures without specific targets nearly impossible. In this study, we employed live imaging, FRAP (Fluorescence Recovery After Photobleaching) analysis, and *in vitro* reconstitution to investigate the properties of targeted proteins. We then used the insights gained (in this case, the immobility of a protein) to guide cryo-ET investigations, leading to the discovery of the Tspan7 transmembrane skeleton. We believe this integrated approach could be useful for discovering other ordered cellular structures.

Acknowledgements

This research was supported by the National Natural Science Foundation of China (grant nos. 32030023, 92354306 and 32330025 to L.Y., 32130054 to H.-W.W., 32200981 to N.L.), Tsinghua-Toyota Joint Research Fund (grant no. 20233930058), Tsinghua University Dushi Program（grant no. 20241080003）and Beijing Municipal Science and Technology Commission, Administrative Commission of Zhongguancun Science Park (grant no. Z221100003422012) to L.Y.. We thank the State Key Laboratory of Membrane Biology and SLSTU-Nikon Biological Imaging Center for facility support in microscopic imaging and data processing. We thank Cryo-EM and High-Performance Computation platforms of Tsinghua University Branch of the National Protein Science Facility, and Shuimu BioSciences Ltd. (Beijing) for the support in cryo-EM data collection. We thank Mr. Xihang Chen (Molecular-Machines&Industries GmbH) for technical support in the optical tweezer system.

Sincere gratitude is expressed towards Dr. Sai Li and Xiaopeng Li for their kind assistance on cryo-ET data processing.

Author contributions

L.Y. and H.-W.W. supervised the project and conceived the experiments. D.J.W. conducted cell experiments, imaging, mutation analysis and statistics. D.J.W. and Y.Z. conducted the *in vitro* reconstitution assays. D.J.W., X.J., Q.Z., N.L.and H-W.W. conducted the cryo-EM analysis. D.J.W., X.J., N.L., and K.X. performed the model building. L.Y., H-W.W., D.J.W., and N.L. wrote the manuscript with input from all authors.

Declarification of interests

L.Y. is the scientific founder of Migrasome Therapeutics Ltd. All other authors declare no competing interests related to this work.

Materials and Methods

Reagents and antibodies

Fibronectin was purchased from Invitrogen (PHE0023) or Sigma (F0895). WGA-TMR (Wheat Germ Agglutinin tetramethylrhodamine conjugate, W849), CellMask Deep Red (C10046) and Lipofectamin-3000 (L3000015) were purchased from Invitrogen. SiR-

568 Actin Kit (CY-SC001) was purchased from Cytoskeleton. Latrunculin A (10010630)
569 was purchased from Cayman. PEI MW40000 was purchased from Yeasen.

570 Lipids including DOPC, DOPE, POPS, cholesterol, 16:0 Biotinyl Cap PE and 18:1 Liss
571 Rhod PE were purchased from Avanti. Streptavidin (85878) was purchased from Sigma.
572 Polybead® Polystyrene Sampler Kit (19822-1) was purchased from Polysciences.

573 Anti-GFP (11814460001) was purchased from Roche. Anti-GAPDH (60004-1-Ig) was
574 purchased from Proteintech.

575 **Plasmid construction**

576 For transient transfection and imaging, the coding sequence of TSPAN7 and other
577 tetraspanins were amplified from rat cDNA through polymerase chain reaction (PCR)
578 and subsequently cloned into a pEGFP-N1 vector (linearized with XhoI and BamHI)
579 through homologous recombination. TSPAN7 constructs with point mutations were
580 generated using a standard site-directed mutagenesis protocol[39]. TSPAN7 constructs
581 with deletions were generated using a standard overlap extension PCR protocol[40].
582 For protein purification, the coding sequence of TSPAN7 was amplified from human
583 cDNA and subsequently cloned into a modified pCAG vector. Briefly, an affinity
584 cassette containing two repeats of Strep-Tag II followed by one FLAG tag was fused to
585 the N-terminal of TSPAN7 and an EGFP tag was fused to the C-terminal of TSPAN7
586 using the linker GGSGGS.

587 **Cell culture and transfection**

588 Adherent cells, including NRK, MGC-803 and MEF cells were cultured at 37 °C and

589 5% CO2 in DMEM high glucose medium supplemented with 10% fetal bovine serum,
590 1% penicillin–streptomycin and 1% Glutamax. 293F cells were cultured in suspension
591 at 37 °C, 5% CO2 and 120 rpm. in SMM293-TII supplemented with 1% penicillin–
592 streptomycin. Electroporation (Amaxa nucleofector, program X-001) was used for the
593 transfection of NRK cells. Lipofectamine-3000 transfection kit was used for the
594 transfection of MGC-803 and MEF. PEI was used for the transfection of 293F cells.

595 **Retraction fiber reconstitution assay via tether pulling**

596 NRK cells at 90% confluence were washed with GPMV buffer (10 mM HEPES, 2 mM
597 $CaCl_2$, 150 mM NaCl, pH 7.4) and incubated with GPMV working buffer (GPMV
598 buffer supplemented with 2 mM DTT and 25 mM formaldehyde before use) for 1 h at
599 37 °C. Supernatant containing GPMV was collected and incubated with 10 μg/ml
600 biotin-PE (and 0.25 μg/ml Rhodamine-PE in some cases) for 10 min at room
601 temperature. Polystyrene beads with 2 μm diameter were incubated with 100 μg/ml
602 streptavidin for 1 h. GPMVs were added to plasma treated glass surface and settled for
603 1 h before the addition of polystyrene beads. Optical tweezer experiments were
604 performed on a Nikon HD25 confocal microscope equipped with MMI CellManipulator.
605 A polystyrene bead was captured by a laser trap and was allowed to contact with a
606 GPMV. By pulling the bead at the opposite direction, a membrane tether was generated.
607 Z-stack images covering GPMV and membrane tether were collected using A1 confocal
608 microscope.

609 **Protein expression and purification**

610 293FT cells were grown to a density of 0.8-1.2 x 10^6 cell/ml and then transfected with

611 2 mg plasmid / L of cell culture using PEI (DNA : PEI = 1: 2.5). 3 days after transfection,
612 cells were harvested by centrifugation at 550 × g. The pellet was washed once with PBS
613 and resuspended in Tris buffer (100 mM Tris, 150 mM NaCl, pH 8.0) supplemented
614 with protease inhibitor. Cells were lysed by grinding 100 times using a glass Dounce
615 homogenizer on ice. The lysate was centrifuged at 30,000 × g for 1 hr and the pellet
616 was resuspended with 10 ml Tris buffer supplemented with protease inhibitor. To
617 extract Tspan7 protein from membrane, 2.5 ml of 10 % (w/v) Fos-Choline-12 was
618 added. The mixture was rotated at 4 °C for 2 hrs and then centrifuged at 12,000 × g for
619 20 min. Supernatant containing extracted protein was loaded to a column containing 1
620 ml pre-balanced strep-tactin beads and incubated for 1 hr at 4 °C on a rotator. The beads
621 were washed with 10 ml wash buffer (100 mM Tris, 150 mM NaCl, 0.1 % (w/v) Fos-
622 Choline-12, pH 8.0). Protein was eluted with 8 ml elution buffer (100 mM Tris, 150
623 mM NaCl, 0.1 % (w/v) Fos-Choline-12, 10 mM desthiobiotin, pH 8.0) and concentrated
624 using a 30 kDa MWCO centrifugal filter.

625 **Liposome preparation**

626 DOPC, DOPE, POPS and cholesterol were mixed at a ratio of 4:2.5:2.5:1, making up 3
627 mg lipids in total. 0.025 % rhodamine-PE was added as a fluorescent indicator. The
628 lipid mixture (prepared in a capped glass vial) was gently dried under a stream of
629 nitrogen and set for 1hr at 37 °C to ensure complete solvent evaporation. The resulting
630 lipid film was hydrated by adding 300 μl HEPES buffer (20 mM HEPES, 150 mM
631 NaCl, pH 7.4) and shaking vigorously at 37 °C for 1 hr. The mixture containing
632 liposomes was transferred into a centrifuge tube and freeze-thawed for at least 10 times

633 by transferring between liquid nitrogen and 42°C water bath. To homogenize liposomes,
634 a polycarbonate membrane with 1 μm pore size was inserted into an extruder and
635 liposomes were passed through for 21 times.

636 **Proteoliposome preparation**

637 Liposomes were kept at 4 °C on a rotator and protected from light during the whole
638 process. First, liposomes were incubated with 0.1 % Fos-Choline-12 for 30 min. Then,
639 purified Tspan7-GFP protein was added at a protein/lipid ratio of 0.01 (for protein-free
640 liposomes, equal amount of wash buffer (100 mM Tris, 150 mM NaCl, 0.1 % (w/v)
641 Fos-Choline-12, pH 8.0) was added). The mixture was incubated for 1 hr. To remove
642 the detergent, 10 – 12 mg of bio-beads / 100 μl liposome were added every hour for 3
643 times. After the third addition of bio-beads, the mixture was stirred overnight. A fourth
644 portion of bio-beads were added on the next day, followed by 1 hr incubation. The
645 supernatant was transferred into a clean centrifuge tube and store in aliquots at -80°C.

646 **GUV preparation and reconstitution**

647 GUVs were prepared via the electroformation method using Vesicle Prep-Pro (Nanion).
648 Before use, ITO (indium tin oxide)-covered glass slides were gently cleaned by liquid
649 soap, triple-washed using distilled water/ethanol and dried under a stream of nitrogen.
650 A rubber ring was stuck onto the ITO-covered side of the slide, creating a confined
651 chamber. 20 μl of proteoliposome was deposited onto the confined glass surface and
652 air-dried. The chamber was gently filled with 280 μl of 300 mM sorbitol and
653 electroformation was then carried out at 0.24 V, 9.9 Hz for 90 min at 37°C. The solution
654 containing GUVs was collected and stored at 4 °C before use.

655 For *in vitro* reconstitution, GUVs were added to a glass-bottom confocal chamber
656 treated with plasma cleanser. The chamber was sealed by parafilm and settled for at
657 least 1.5 h before imaging by a confocal microscope.

658 **Imaging and staining**

659 Cells were seeded on 10 μg/ml fibronectin coated confocal chamber (Cellvis) and
660 transferred to a Nikon A1 HD25 confocal microscope equipped with a live cell imaging
661 system. Images were acquired using a 100× objective at 1024 × 1024 pixels. For long-
662 term time-lapse experiments, cells were allowed to migrate for about 6 hrs before
663 imaging. Images were acquired at 2 min interval for indicated time periods. For
664 confocal snapshot images and FRAP assays, cells were allowed to migrate for about 16
665 hrs before imaging. An additional staining step was performed before imaging in some
666 experiments. Specifically, cells were incubated with 1 μg/ml WGA-TMR for 10min,
667 1.25 μg/ml CellMask Deep Red for 10 min or 1 μM SiR-actin for 1h before imaging.

668 **FRAP assay and data processing**

669 For each cell analyzed, 7 ROIs (Region Of Interest) were defined: 3 stimulation ROIs
670 (1.6 μm diameter), 3 reference ROIs (1.6 μm diameter) and 1 background ROI. The
671 experiment contains three phases: first, two frames were captured before stimulation;
672 next, stimulation ROIs were bleached with 100% 488 nm laser for 1.5 s; finally, a 5 min
673 time-lapse movie was recorded after bleaching. Data processing was performed using
674 the NIS-Elements software. First, alignment was performed to correct XY motions.
675 Then, the mean fluorescent signals of 7 ROIs over time were measured. Next, the
676 fluorescent signals of stimulation ROIs were subjected to background correction and

677 reference correction. Finally, all datasets were linearly normalized to the [0, 100] range.
678 The largest value of each dataset was defined as 100% and 0 was defined as 0%.

679 **Cryo-EM specimen preparation**

680 Quantifoil R1.2/1.3 Au-grids (200 mesh) were coated with homemade graphene film[41]
681 and glow-discharged for 15 seconds (Harrick Plasma, low-power mode). Afterwards,
682 the EM grids were placed in a 35-mm Ibidi μ-Dish under ultraviolet illumination for 10
683 minutes. Next, human plasma fibronectin (FC010, Millipore, USA) solution (10 μg/ml
684 in PBS buffer) was dropped onto the EM grids and incubated for 40 minutes at 37 °C.
685 The fibronectin solution was then removed, and 1.2×10^5 NRK cells were seeded on
686 the EM grids and cultured overnight at 37°C and 5% CO_2. After a 14-16 hour culture,
687 we imaged the EM grids using a confocal light microscope with a 100× magnification
688 lens to obtain a grid atlas. The EM grids with cultured cells were then gently picked up
689 with tweezers, and 3 μL of nanogold particle solution (10 nm in diameter; Aurion, the
690 Netherlands) was added onto each grid. We then plunge-froze the grids using a Leica
691 EM GP. Grids were blotted from the back using the Leica EM GP at 37°C and 90%
692 humidity with a blotting time of 8-10 seconds. Finally, the grids were transferred into
693 liquid nitrogen for storage, ready for loading into the cryo transmission electron
694 microscope.

695 **Single-particle cryo-EM data collection and analysis**

696 The single-particle cryo-EM datasets for Tspan4-GFP and Tspan7-GFP retraction
697 fibers were collected using a Thermo Fisher Scientific Titan Krios (300 kV) TEM,

698 equipped with a K3 camera (Gatan, Inc.) and an energy filter. We collected 99
699 micrographs for Tspan4 and 103 micrographs for Tspan7 samples at a magnification of
700 18000×, with a defocus range of -1.5 to -2.0 μm. Each micrograph was dose-
701 fractionated into 32 frames with a cumulative dose of 50 $e^-/Å^2$ and a pixel size of 1.56
702 Å. The micrographs were motion-corrected using MotionCor2[42] and then imported into
703 Relion[43] for data processing. We used CTFFIND4 to estimate the CTF parameters[44].
704 We manually picked 1502 particles for the Tspan4 samples and 1570 particles for the
705 Tspan7 samples for the subsequent two-dimensional classification, using identical
706 parameters.

707 **Cryo-electron tomography data collection and reconstruction**

708 Cryo-electron tomography (cryo-ET) tilt series of retraction fibers were collected on a
709 Titan Krios microscope operated at 300 kV (Thermo Fisher Scientific) equipped with
710 a GIF Quantum post-column energy filter (Gatan) and a K3 direct detector camera
711 (Gatan). Data were recorded in dose-fractionation mode using SerialEM software[45].
712 Tilt-series were collected using a dose symmetric scheme[46] in nanoprobe mode, with a
713 calibrated pixel size of 1.36 Å, a defocus range of -4.5 to -6.5 μm, a tilt increment of
714 3°, and an imaging dose of 3 $e^-/Å^2$ for all tilts. The tilt range was from +60° to -60°
715 starting from 0°, resulting in a total dose of ～123 $e^-/Å^2$. We collected 12 tilt series for
716 the Tspan4-GFP retraction fibers, 77 tilt series for the Tspan7-GFP retraction fibers,
717 and 82 tilt series for the LatA-treated Tspan7-GFP retraction fibers, respectively.

718 The tilt series were imported to Warp software[47] for motion correction as well as CTF

719 estimation. The corrected tilt series were firstly aligned in IMOD[48] using a combination
720 of patch-tracking and gold fiducial markers for tracking, and then the final alignment
721 was performed using the linear interpolation option. Aligned images were binned by a
722 factor of 4 to a pixel size of 5.44 Å for sub-tomogram averaging.

723 For subtomogram averaging of Tspan7-GFP retraction fiber, the retraction fibers were
724 first traced in Dynamo[49] package. In the Dynamo model generation interface, we
725 manually selected the extremal points of straight segments along each retraction fiber
726 to define the central line ‘‘backbone’’. Bent regions of the retraction fibers were
727 discarded. Subsequently, we used the Dynamo filament model with torsion type for
728 generating subtomograms. The parameters *subunits_dz* and *subunits_dphi* were set to
729 12 pixels and 30°, repectively, to account for the helical rise of the retraction fibers and
730 to reduce the effect of the missing wedge in subtomogram averaging[50]. Subtomograms
731 (4 times binned, with a box size of 128^3 pixels) were cropped using Dynamo with the
732 model-defined positions, and initial Euler angles were generated relative to filament
733 axes with extra in-plane rotations derived from torsion angles.

734 Reference-free subtomogram averaging/refinement was performed using Dynamo.
735 Initial reference was generated by averaging subtomograms (4 times binned) from 3
736 retraction fibers without alignment. A cylindrical mask was generated in Dynamo
737 according to the initial average, and used as alignment mask. Other masks were left as
738 default. The resulting average of the 3 retraction fibers was used to align all 2208
739 subtomograms extracted from 29 retraction fibers.

740 **Model building of Tspan7 spiral structure**

741 We used the MMSeq2[51] to generate Multiple Sequence Alignments (MSAs) for the
742 Tspan7 dimer. Following this, we conducted network predictions using AlphaFold-
743 Multimer (version 2.3), employing the default 5-model parameter settings [38] and
744 utilizing 17 distinct random seeds. This process ultimately yielded 85 predicted models
745 of the Tspan7 dimer, which could be clustered into 5 classes based on their interaction
746 interfaces.

747 To clearly illustrate the interaction modes of these dimer models, we selected one
748 representative structure from each of the five classes of the Tspan7 dimer (dimers 1-5).
749 Upon aligning one monomer of each dimer using the *matchmarker* function in
750 ChimeraX, we found that dimer 1 and dimer 2 were arranged in a line, which is
751 consistent with the feature of the TEM density map of Tspan7 forming a long chain.
752 We then placed all these 5 dimers into the partitioned helical asymmetric unit density,
753 aligning the "V" shape opening of Tspan7 with the orientation of the membrane
754 curvature (Figure S4, S5). The correlation calculation was then performed in ChimeraX.

755 We used the interaction interfaces from dimer1 and dimer2 to build the Tspan7 spiral
756 model, placing them into the long chains of Tspan7 spiral density map. Consequently,
757 we maintained the interaction interfaces unchanged while manually adjusting the angle
758 between the monomers to modify the distance between their transmembrane regions,
759 thereby reducing the apparent clash. The spiral model was then generated using the
760 spiral parameters (rise 65 Å, twist 3.14, 6-start), which were inferred from the

761 subtomogram averaging density map.

762

763 **Supplemental information**

764 Document S1. Figure S1-S7

765 Video S1. *In vitro* reconstitution using protein-free GUV, related to Figure 2B

766 Video S2. *In vitro* reconstitution using Tspan7-GFP-embedded GUV, related to Figure
767 2C

768 Video S3. Tomogram of retraction fiber from NRK cells expressing Tspan4-GFP,
769 related to Figure 4E (left).

770 Video S4. Tomogram of retraction fiber from NRK cells expressing Tspan7-GFP,
771 related to Figure 4E (middle).

772 Video S5. Tomogram of retraction fiber from NRK cells expressing Tspan7-HA, related
773 to Figure 4E (right).

774 Video S6. The dynamics of SiR-actin and Tspan7-GFP on retraction fibers, related to
775 Figure 5E

776 Video S7. Tomogram of retraction fiber from NRK cells expressing Tspan7-GFP and
777 treated with 2 μM LatA, related to Figure 5J.

778 Video S8. Tomogram of retraction fiber from NRK cells expressing Tspan7 3M-GFP,
779 related to Figure 6D.

References

1. Mill, P., Christensen, S.T., and Pedersen, L.B. (2023). Primary cilia as dynamic and diverse signalling hubs in development and disease. Nature Reviews Genetics *24*, 421-441. 10.1038/s41576-023-00587-9.
2. Mattila, P.K., and Lappalainen, P. (2008). Filopodia: molecular architecture and cellular functions. Nature Reviews Molecular Cell Biology *9*, 446-454. 10.1038/nrm2406.
3. Buszczak, M., Inaba, M., and Yamashita, Y.M. (2016). Signaling by Cellular Protrusions: Keeping the Conversation Private. Trends in Cell Biology *26*, 526-534. 10.1016/j.tcb.2016.03.003.
4. Jacquemet, G., Hamidi, H., and Ivaska, J. (2015). Filopodia in cell adhesion, 3D migration and cancer cell invasion. Current Opinion in Cell Biology *36*, 23-31. https://doi.org/10.1016/j.ceb.2015.06.007.
5. Wang, C., Xie, B., Yin, S., Cao, J., Huang, J., Jin, L., Du, G., Zhai, X., Zhang, R., Li, S., et al. (2023). Induction of filopodia formation by α-Actinin-2 via RelA with a feedforward activation loop promoting overt bone marrow metastasis of gastric cancer. Journal of Translational Medicine *21*, 399. 10.1186/s12967-023-04156-w.
6. Bischoff, M.C., Lieb, S., Renkawitz-Pohl, R., and Bogdan, S. (2021). Filopodia-based contact stimulation of cell migration drives tissue morphogenesis. Nature Communications *12*, 791. 10.1038/s41467-020-20362-2.
7. Zhang, C., Brunt, L., Ono, Y., Rogers, S., and Scholpp, S. (2024). Cytoneme-mediated transport of active Wnt5b–Ror2 complexes in zebrafish. Nature *625*, 126-133. 10.1038/s41586-023-06850-7.
8. Taylor, A.C., and Robbins, E. (1963). Observations on microextensions from the surface of isolated vertebrate cells. Developmental Biology *7*, 660-673. https://doi.org/10.1016/0012-1606(63)90150-7.
9. Lee, S.Y., Choi, S.H., Lee, M.S., Kurmashev, A., Lee, H.N., Ko, Y.G., Lee, K., Jeong, S., Seong, J., Kang, J.H., and Kim, H. (2021). Retraction fibers produced by fibronectin-integrin α5β1 interaction promote motility of brain tumor cells. Faseb j *35*, e21906. 10.1096/fj.202100452RR.
10. Porter, K.R., Claude, A., and Fullam, E.F. (1945). A STUDY OF TISSUE CULTURE CELLS BY ELECTRON MICROSCOPY : METHODS AND PRELIMINARY OBSERVATIONS. J Exp Med *81*, 233-246. 10.1084/jem.81.3.233.
11. Ma, L., Li, Y., Peng, J., Wu, D., Zhao, X., Cui, Y., Chen, L., Yan, X., Du, Y., and Yu, L. (2015). Discovery of the migrasome, an organelle mediating release of cytoplasmic contents during cell migration. Cell Res *25*, 24-38. 10.1038/cr.2014.135.
12. Jiang, D., Jiang, Z., Lu, D., Wang, X., Liang, H., Zhang, J., Meng, Y., Li, Y., Wu, D., Huang, Y., et al. (2019). Migrasomes provide regional cues for organ morphogenesis during zebrafish gastrulation. Nat Cell Biol *21*, 966-977. 10.1038/s41556-019-0358-6.

13. Zhu, M., Zou, Q., Huang, R., Li, Y., Xing, X., Fang, J., Ma, L., Li, L., Yang, X., and Yu, L. (2021). Lateral transfer of mRNA and protein by migrasomes modifies the recipient cells. Cell Res *31*, 237-240. 10.1038/s41422-020-00415-3.
14. Jiao, H., Jiang, D., Hu, X., Du, W., Ji, L., Yang, Y., Li, X., Sho, T., Wang, X., Li, Y., et al. (2021). Mitocytosis, a migrasome-mediated mitochondrial quality-control process. Cell *184*, 2896-2910 e2813. 10.1016/j.cell.2021.04.027.
15. Zhang, C., Li, T., Yin, S., Gao, M., He, H., Li, Y., Jiang, D., Shi, M., Wang, J., and Yu, L. (2022). Monocytes deposit migrasomes to promote embryonic angiogenesis. Nat Cell Biol *24*, 1726-1738. 10.1038/s41556-022-01026-3.
16. Kim, J., Jo, H., Hong, H., Kim, M.H., Kim, J.M., Lee, J.-K., Heo, W.D., and Kim, J. (2015). Actin remodelling factors control ciliogenesis by regulating YAP/TAZ activity and vesicle trafficking. Nature Communications *6*, 6781. 10.1038/ncomms7781.
17. Routledge, D., Rogers, S., Ono, Y., Brunt, L., Meniel, V., Tornillo, G., Ashktorab, H., Phesse, T.J., and Scholpp, S. (2022). The scaffolding protein flot2 promotes cytoneme-based transport of wnt3 in gastric cancer. eLife *11*, e77376. 10.7554/eLife.77376.
18. Boucheix, C., and Rubinstein, E. (2001). Tetraspanins. Cellular and Molecular Life Sciences CMLS *58*, 1189-1205. 10.1007/PL00000933.
19. Hemler, M.E. (2005). Tetraspanin functions and associated microdomains. Nature Reviews Molecular Cell Biology *6*, 801-811. 10.1038/nrm1736.
20. Huang, Y., Zhang, X., Wang, H.-W., and Yu, L. (2022). Assembly of Tetraspanin-enriched macrodomains contains membrane damage to facilitate repair. Nature Cell Biology *24*, 825-832. 10.1038/s41556-022-00920-0.
21. Zijlstra, A., Lewis, J., DeGryse, B., Stuhlmann, H., and Quigley, J.P. (2008). The Inhibition of Tumor Cell Intravasation and Subsequent Metastasis via Regulation of In Vivo Tumor Cell Motility by the Tetraspanin CD151. Cancer Cell *13*, 221-234. 10.1016/j.ccr.2008.01.031.
22. Lammerding, J., Kazarov, A.R., Huang, H., Lee, R.T., and Hemler, M.E. (2003). Tetraspanin CD151 regulates α6β1 integrin adhesion strengthening. Proceedings of the National Academy of Sciences *100*, 7616-7621. 10.1073/pnas.1337546100.
23. Rubinstein, E., Le Naour, F., Lagaudrière-Gesbert, C., Billard, M., Conjeaud, H., and Boucheix, C. (1996). CD9, CD63, CD81, and CD82 are components of a surface tetraspan network connected to HLA-DR and VLA integrins. European Journal of Immunology *26*, 2657-2665. https://doi.org/10.1002/eji.1830261117.
24. Menager, M.M., and Littman, D.R. (2016). Actin Dynamics Regulates Dendritic Cell-Mediated Transfer of HIV-1 to T Cells. Cell *164*, 695-709. 10.1016/j.cell.2015.12.036.
25. Runge, K.E., Evans, J.E., He, Z.-Y., Gupta, S., McDonald, K.L., Stahlberg, H., Primakoff, P., and Myles, D.G. (2007). Oocyte CD9 is enriched on the microvillar membrane and required for normal microvillar shape and

867 distribution. Developmental Biology *304*, 317-325.
868 https://doi.org/10.1016/j.ydbio.2006.12.041.
869 26. Bassani, S., Cingolani, L.A., Valnegri, P., Folci, A., Zapata, J., Gianfelice, A.,
870 Sala, C., Goda, Y., and Passafaro, M. (2012). The X-linked intellectual disability
871 protein TSPAN7 regulates excitatory synapse development and AMPAR
872 trafficking. Neuron *73*, 1143-1158. 10.1016/j.neuron.2012.01.021.
873 27. Blumenthal, A., Giebel, J., Ummanni, R., Schlüter, R., Endlich, K., and Endlich,
874 N. (2012). Morphology and migration of podocytes are affected by CD151
875 levels. American Journal of Physiology-Renal Physiology *302*, F1265-F1277.
876 10.1152/ajprenal.00468.2011.
877 28. Dharan, R., Goren, S., Cheppali, S.K., Shendrik, P., Brand, G., Vaknin, A., Yu,
878 L., Kozlov, M.M., and Sorkin, R. (2022). Transmembrane proteins tetraspanin
879 4 and CD9 sense membrane curvature. Proceedings of the National Academy of
880 Sciences *119*, e2208993119. 10.1073/pnas.2208993119.
881 29. Huang, Y., Zucker, B., Zhang, S., Elias, S., Zhu, Y., Chen, H., Ding, T., Li, Y.,
882 Sun, Y., Lou, J., et al. (2019). Migrasome formation is mediated by assembly of
883 micron-scale tetraspanin macrodomains. Nat Cell Biol *21*, 991-1002.
884 10.1038/s41556-019-0367-5.
885 30. Dharan, R., Huang, Y., Cheppali, S.K., Goren, S., Shendrik, P., Wang, W., Qiao,
886 J., Kozlov, M.M., Yu, L., and Sorkin, R. (2023). Tetraspanin 4 stabilizes
887 membrane swellings and facilitates their maturation into migrasomes. Nat
888 Commun *14*, 1037. 10.1038/s41467-023-36596-9.
889 31. Yáñez-Mó, M., Barreiro, O., Gordon-Alonso, M., Sala-Valdés, M., and
890 Sánchez-Madrid, F. (2009). Tetraspanin-enriched microdomains: a functional
891 unit in cell plasma membranes. Trends in Cell Biology *19*, 434-446.
892 https://doi.org/10.1016/j.tcb.2009.06.004.
893 32. Charrin, S., Manié, S., Thiele, C., Billard, M., Gerlier, D., Boucheix, C., and
894 Rubinstein, E. (2003). A physical and functional link between cholesterol and
895 tetraspanins. European Journal of Immunology *33*, 2479-2489.
896 https://doi.org/10.1002/eji.200323884.
897 33. Wu, X.-R., Kong, X.-P., Pellicer, A., Kreibich, G., and Sun, T.-T. (2009).
898 Uroplakins in urothelial biology, function, and disease. Kidney International *75*,
899 1153-1165. https://doi.org/10.1038/ki.2009.73.
900 34. Oostergetel, G.T., Keegstra, W., and Brisson, A. (2001). Structure of the major
901 membrane protein complex from urinary bladder epithelial cells by cryo-
902 electron crystallography1 1Edited by W. Baumeister. J Mol Biol *314*, 245-252.
903 https://doi.org/10.1006/jmbi.2001.5128.
904 35. Tamura, K., Stecher, G., and Kumar, S. (2021). MEGA11: Molecular
905 Evolutionary Genetics Analysis Version 11. Molecular biology and evolution
906 *38*, 3022-3027. 10.1093/molbev/msab120.
907 36. Jones, D.T., Taylor, W.R., and Thornton, J.M. (1992). The rapid generation of
908 mutation data matrices from protein sequences. Computer applications in the
909 biosciences : CABIOS *8*, 275-282. 10.1093/bioinformatics/8.3.275.
910 37. Jumper, J., Evans, R., Pritzel, A., Green, T., Figurnov, M., Ronneberger, O.,

Tunyasuvunakool, K., Bates, R., Žídek, A., Potapenko, A., et al. (2021). Highly accurate protein structure prediction with AlphaFold. Nature *596*, 583-589. 10.1038/s41586-021-03819-2.

38. Evans, R., O'Neill, M., Pritzel, A., Antropova, N., Senior, A., Green, T., Žídek, A., Bates, R., Blackwell, S., Yim, J., et al. (2021). Protein complex prediction with AlphaFold-Multimer. bioRxiv, 2021.2010.2004.463034. 10.1101/2021.10.04.463034.
39. Zheng, L., Baumann U Fau - Reymond, J.-L., and Reymond, J.L. An efficient one-step site-directed and site-saturation mutagenesis protocol.
40. Nelson, M.D., and Fitch, D.H.A. (2011). Overlap Extension PCR: An Efficient Method for Transgene Construction. In Molecular Methods for Evolutionary Genetics, V. Orgogozo, and M.V. Rockman, eds. (Humana Press), pp. 459-470. 10.1007/978-1-61779-228-1_27.
41. Zheng, L., Liu, N., Gao, X., Zhu, W., Liu, K., Wu, C., Yan, R., Zhang, J., Gao, X., Yao, Y., et al. (2023). Uniform thin ice on ultraflat graphene for high-resolution cryo-EM. Nature Methods *20*, 123-130. 10.1038/s41592-022-01693-y.
42. Zheng, S.Q., Palovcak, E., Armache, J.-P., Verba, K.A., Cheng, Y., and Agard, D.A. (2017). MotionCor2: anisotropic correction of beam-induced motion for improved cryo-electron microscopy. Nature Methods *14*, 331-332. 10.1038/nmeth.4193.
43. Zivanov, J., Nakane, T., Forsberg, B.O., Kimanius, D., Hagen, W.J., Lindahl, E., and Scheres, S.H. (2018). New tools for automated high-resolution cryo-EM structure determination in RELION-3. Elife *7*. 10.7554/eLife.42166.
44. Rohou, A., and Grigorieff, N. (2015). CTFFIND4: Fast and accurate defocus estimation from electron micrographs. J Struct Biol *192*, 216-221. 10.1016/j.jsb.2015.08.008.
45. Mastronarde, D.N. (2005). Automated electron microscope tomography using robust prediction of specimen movements. Journal of Structural Biology *152*, 36-51. https://doi.org/10.1016/j.jsb.2005.07.007.
46. Hagen, W.J.H., Wan, W., and Briggs, J.A.G. (2017). Implementation of a cryo-electron tomography tilt-scheme optimized for high resolution subtomogram averaging. Journal of Structural Biology *197*, 191-198. https://doi.org/10.1016/j.jsb.2016.06.007.
47. Tegunov, D., and Cramer, P. (2019). Real-time cryo-electron microscopy data preprocessing with Warp. Nature Methods *16*, 1146-1152. 10.1038/s41592-019-0580-y.
48. Kremer, J.R., Mastronarde, D.N., and McIntosh, J.R. (1996). Computer Visualization of Three-Dimensional Image Data Using IMOD. Journal of Structural Biology *116*, 71-76. https://doi.org/10.1006/jsbi.1996.0013.
49. Castaño-Díez, D., Kudryashev, M., Arheit, M., and Stahlberg, H. (2012). Dynamo: A flexible, user-friendly development tool for subtomogram averaging of cryo-EM data in high-performance computing environments. Journal of Structural Biology *178*, 139-151.

https://doi.org/10.1016/j.jsb.2011.12.017.

50. Wan, W., and Briggs, J.A.G. (2016). Chapter Thirteen - Cryo-Electron Tomography and Subtomogram Averaging. In Methods in Enzymology, R.A. Crowther, ed. (Academic Press), pp. 329-367. https://doi.org/10.1016/bs.mie.2016.04.014.

51. Steinegger, M., and Söding, J. (2017). MMseqs2 enables sensitive protein sequence searching for the analysis of massive data sets. Nature Biotechnology *35*, 1026-1028. 10.1038/nbt.3988.